



Study on the Effect of SEMS on the As-Cast Structure of Steel in Thin Slab Continuous Casting Using an Equiaxed-Columnar Solidification Model

CHANGJUN WANG, ZHONGQIU LIU, and BAOKUAN LI

Strand electromagnetic stirring (SEMS) is widely applied in thin slab continuous casting to improve the equiaxed crystal ratio (ECR) of steel. To provide a deeper insight into the role of SEMS in controlling the flow pattern, superheat transportation, macrosegregation, and as-cast structure in the whole strand. A three-phase equiaxed-columnar solidification model was developed to predict the solidification process. The anisotropic permeability of directional columnar structures was integrated into the model by tracking the columnar growing direction. Numerical results showed that two recirculating flow regions came into being under the one-way moving magnetic field induced by the SEMS. The upward recirculating flow deflected the nozzle jet and assembled a superheat melt impinging towards the narrow face under the electromagnetic stirring. Level velocity and level height in the stirring direction were disturbed by the upward flow. Equiaxed grains formed in the stirring direction were less than the volume fraction on the other side. The one-way magnetic field also caused an asymmetric distribution of equiaxed grains in the thickness direction. Applying SEMS was beneficial to the improvement of ECR. The ECR in the strand was 4 pct in the absence of electromagnetic stirring, and it increased to 17.4 pct after applying the SEMS.

<https://doi.org/10.1007/s11663-023-02904-3>

© The Minerals, Metals & Materials Society and ASM International 2023

I. INTRODUCTION

THIN slab continuous casting (TSCC) is rapidly becoming the cutting-edge process for producing thin gauge, high-value steel products in the iron and steel industry. Its greatest advantage over conventional slab casting is integrating near-net shape casting with a rolling mill.^[1] To obtain high-quality steel at high casting speed, severe problems such as turbulent flow inside the mold, coarse as-cast structures, and chemical inhomogeneity need to be prevented. Various thin slab casting and rolling technologies, including funnel-type mold, bifurcated submerged entry nozzle, dynamic liquid core reduction, and electromagnetic control, have been designed to improve the surface and internal quality of continuous casting steel.^[2]

Electromagnetic braking (EMBr) is vital for stabilizing turbulent flow in the mold. A static external magnetic field is applied across the mold cavity to generate Lorentz force, which is in the opposite direction to the steel flow. The vortex flow can be significantly suppressed, and plug-like flow forms in the lower part of the mold.^[3] Although the working principle is easy to understand, long-time practical experience reveals that EMBr sometimes worsens the flow pattern and fluctuation of the slag-melt interface. One reason is that the position of the transverse magnetic field is difficult to adjust in real time according to the steel flow pattern inside the mold cavity. Applying a transverse magnetic field below the steel jet can cause the jet to flow upward and deliver more superheat to the meniscus.^[4] Applying the transverse magnetic field across the meniscus can slow down the surface flow and therefore reduce the formation of mold slag droplets.^[5] The other important reason is that the magnetic field strength must be maintained within a reasonable range. Excessive magnetic field strength near the meniscus can slow the meniscus velocity too much and aggravate the capture of particles beneath subsurface hooks.^[6] Vakhrušev *et al.*^[7] presented the formation and evolution regimes of the reverse meniscus flow under the influence of magnetic field strength. The relationship between the flow structure and magnetic field strength was remarkably concluded. The state of the mold slag film between the

CHANGJUN WANG, ZHONGQIU LIU, and BAOKUAN LI are with the Key Laboratory for Ecological Metallurgy of Multimetallurgical Mineral (Ministry of Education), Northeastern University, Shenyang 110819, P.R. China and also with the School of Metallurgy, Northeastern University, Shenyang 110819, P.R. China. Contact e-mail: liuzq@smm.neu.edu.cn; libk@smm.neu.edu.cn

Manuscript submitted April 17, 2023; accepted August 24, 2023.

Article published online September 5, 2023.

strand surface and cavity copper can also influence the application of EMBr. Liu *et al.*^[8] found that electrically-conducting boundary conditions could predict more electromagnetic force than insulated walls. It means that considering the solidified steel shell is crucial for predicting flow fields in a continuous casting process with EMBr.

Strand electromagnetic stirring (SEMS) can improve the equiaxed crystal ratio (ECR) and chemical homogeneity, which are important factors reflecting the internal quality and mechanical properties of continuous casting steel. The cooling time of the molten steel will increase on account of the produced vertical recirculating flow across the strand width. This is conducive to the undercooling nucleation and the formation of equiaxed grains.^[9] Gong *et al.*^[10] studied the effects of stirring current, stirring frequency, and stirrer configuration on the electromagnetically driven flow in a vertical curved continuous slab caster. The results showed that the flow field driven by electromagnetic stirring was beneficial to the increase of ECR. Furthermore, Wang *et al.*^[11] found that the vertical recirculating flow in the strand was beneficial to the dissipation of superheat and promoting a uniform solidified steel shell. Recent numerical research showed that applying mold electromagnetic stirring could also improve the formation of equiaxed grains.^[12] The mold electromagnetic stirring was more effective in impacting crystal fragmentation than undercooling nucleation.

Continuous casting is a complicated physical process, including heat transfer, solidification, turbulent flow, particle removal, segregation, and as-cast structure. Solidification is the foremost function in the process, which coexists with segregation and as-cast structure. The multiphase volume-averaged solidification model is the most flexible approach to simultaneously predict the above solidification qualities. Previous work has paid particular attention to the development and validation of the model based on benchmark solidification experiments.^[13] Liu *et al.*^[14] built an alloy experiment system to investigate the solidified structure evolution during the cold strip feeding process using the three-phase mixed columnar-equiaxed solidification model. The results showed that cold strip feeding could improve the solidified structure quality. Recently, Wang *et al.*^[15] integrated the columnar growing direction into the columnar-equiaxed solidification model and proposed a novel columnar tip tracking algorithm. The improved model was validated by comparing the numerical results to the solidification benchmark experiment designed by SIMAP Laboratory.^[16] When predicting an industry solidification process, much of the literature concerns steel ingot casting.^[17] The segregation caused by crystal sedimentation, quasi A-segregates in the middle region, and discontinued positive-negative segregation just below the hot top were successfully predicted.^[18] Research investigating the continuous casting process has become available over the past two decades. The fundamental mechanisms of feeding, bulging, and mechanical soft reduction on the centerline macrosegregation of steel strand was investigated.^[19] Jiang and Zhu^[20] first studied the solidification structure and

macrosegregation in a steel billet by applying dual electromagnetic stirrings. Results showed that increasing the intensity of the mold electromagnetic stirring had no significant influence on ECR. The final electromagnetic stirring could improve the billet center segregation only within a specific range of stirring pool width.^[21] Effects of thermal shrinkage on the slab center segregation were analyzed by interpreting a thermal shrinkage model into the volume-averaged solidification model.^[22] Guan *et al.*^[23] proposed a novel back-diffusion model using the Won-Thomas model to predict the carbon solute distribution in the steel bloom. These studies indicate that the multiphase volume-averaged solidification model can provide valuable insights into the internal solidification state of continuous casting steel. However, few researchers have addressed the numerical prediction of the as-cast structure and macrosegregation in a TSCC process based on this approach. The combined function of EMBr and SEMS on internal qualities remains unclear.

In this study, a volume-averaged equiaxed-columnar solidification model was developed to predict the solidification process in TSCC. A modified columnar-tip tracking algorithm was adopted based on the authors' previous work, in which columnar growing direction was integrated into the solidification model. The anisotropic permeability of the directional columnar structure was further considered to increase the calculation accuracy of the flow field in the mushy zone. The main objective of this study focused on the role of SEMS controlling the flow pattern, superheat transportation, macrosegregation, and as-cast structure in the thin slab continuous casting process.

II. NUMERICAL MODEL DESCRIPTION

A. Overview of the Equiaxed-columnar Solidification Model

The present equiaxed-columnar solidification model records the columnar growing direction to improve the columnar-tip tracking algorithm. Anisotropic permeability is further integrated into this model to describe the drag force in the directional columnar structure. Furthermore, the combined effects of static and moving magnetic fields on solidification are considered. Induced magnetic fields related to the turbulent flow are neglected due to a very low magnetic Reynolds number. The electric potential method is adopted to calculate the braking force induced by EMBr. Time-averaged Lorentz force and Joule heat generated from SEMS are interpolated directly into the computational domain for good convergence. The governing equations and source terms of the model are summarized in Table I, in which the subscripts i and j indicate different phases.

Each cell is marked with an index to represent the solidification status of columnar crystals. The advancement of the columnar front is tracked explicitly at the end of every time step. A columnar-tip cell will be marked as a columnar-trunk cell when the average columnar length exceeds the reference length of the cell.

Table I. A Summary of the Equiaxed-Columnar Solidification Model

Governing Equations

1. Mass Equation	$\frac{\partial}{\partial t}(f_i \rho) + \nabla \cdot (f_i \rho \mathbf{v}_i) = M_{ji}$	(1)
2. Momentum Equation	$\frac{\partial}{\partial t}(f_i \rho \mathbf{v}_i) + \nabla \cdot (f_i \rho \mathbf{v}_i \mathbf{v}_i) = -f_i \nabla p + \nabla \cdot \boldsymbol{\tau}_i + f_i \tilde{\rho}_i \mathbf{g} + \mathbf{F}_{ji} + f_i \mathbf{F}_L$ with $\mathbf{g} = [0 \quad 0 \quad -9.8]^T$	(2)
3. Species Equation	$\frac{\partial}{\partial t}(f_i \rho c_i) + \nabla \cdot (f_i \rho \mathbf{v}_i c_i) = \nabla \cdot (f_i \rho D_i \nabla c_i) + C_{ji}$	(3)
4. Enthalpy Equation	$\frac{\partial}{\partial t}(f_i \rho h_i) + \nabla \cdot (f_i \rho \mathbf{v}_i h_i) = \nabla \cdot (f_i k_i \nabla T_i) + Q_{ji} + f_i Q_J$	(4)
5. Transport of Equiaxed Nucleus	$\frac{\partial}{\partial t} n_c + \nabla \cdot (\mathbf{v}_c n_c) = N_{nu} + N_{frag}$	(5)
6. External Electromagnetic Field	$\nabla \times \mathbf{E} = -\frac{\partial \mathbf{B}}{\partial t}$ $\nabla \times \mathbf{H} = \mathbf{J}$ with $\mathbf{H} = \mathbf{B}/\mu_{mag}$ and $\mathbf{J} = \sigma \mathbf{E}$	(6) (7)
	$\nabla \cdot \mathbf{B} = 0$	(8)
7. Electric Potential Method	$\nabla \cdot (\sigma_{mix} \nabla \varphi) = \nabla \cdot [\sigma_{mix} \cdot (\mathbf{v}_{mix} \times \mathbf{B})]$	(9)

Source Terms

Mass Transfer Rate	$M_{lc} = \begin{cases} \Phi_{imp}^c \rho v_{Re} S_c^{trunk} & \text{trunks} \\ \Phi_{imp}^c \rho (v_{Re} S_c^{tip} + v_{c,tip} n_c \pi R_{tip}^2) & \text{tips} \end{cases}$	(10)
	$M_{lc} = \Phi_{imp}^c \rho v_{Re} S_c$	(11)
	$M_{cc} = -\gamma \rho (\mathbf{v}_l - \mathbf{v}_c) \cdot \nabla c_l$	(12)
Momentum Exchange Terms	$\mathbf{F}_{lc} = \mu_l^2 \mathbf{K}_{lc}^{-1} (\mathbf{v}_l - \mathbf{v}_c) + \mathbf{v}^* M_{lc}$ with $\mathbf{v}^* = \begin{cases} \mathbf{v}_l & \text{solidification} \\ \mathbf{v}_c & \text{melting} \end{cases}$	(13)
	$\mathbf{F}_{lc} = K_{lc} (\mathbf{v}_l - \mathbf{v}_c) + \mathbf{v}^* M_{lc}$ with $\mathbf{v}^* = \begin{cases} \mathbf{v}_l & \text{solidification} \\ \mathbf{v}_c & \text{melting} \end{cases}$	(14)
	$\mathbf{F}_{cc} = K_{cc} (\mathbf{v}_c - \mathbf{v}_e) + \mathbf{v}_c M_{cc}$ with $K_{cc} = \begin{cases} 0 & f_c < 0.2 \\ 2 \times 10^9 & f_c \geq 0.2 \end{cases} \pi$	(15)
	$\mathbf{F}_{L,EMBr} = \mathbf{j} \times \mathbf{B}$ with $\mathbf{j} = \sigma_{mix} (-\nabla \varphi + \mathbf{v}_{mix} \times \mathbf{B})$	(16)
	$\mathbf{F}_{L,SEMS} = \frac{1}{2} \text{Re}(\mathbf{J} \times \mathbf{B})$	(17)
Species Transfer Rate	$C_{lc} = \begin{cases} c_s^* M_{lc} + \rho S_c D_c \frac{(c_s^* - c_c)}{R_c/2} & \text{solidification} \\ c_c M_{lc} & \text{melting} \end{cases}$	(18)
	$C_{lc} = \begin{cases} c_s^* M_{lc} + \rho S_c D_c \frac{(c_s^* - c_c)}{R_c/2} & \text{solidification} \\ c_c M_{lc} & \text{melting} \end{cases}$	(19)
	$C_{cc} = c_c M_{cc}$	(20)
Enthalpy Transfer Terms	$Q_{lc} = H^* f_{lc} (T_l - T_c) + h^* M_{lc}$ with $h^* = \begin{cases} h_l & \text{solidification} \\ h_c & \text{melting} \end{cases}$	(21)
	$Q_{lc} = H^* f_{lc} (T_l - T_c) + h^* M_{lc}$ with $h^* = \begin{cases} h_l & \text{solidification} \\ h_c & \text{melting} \end{cases}$	(22)
	$Q_{cc} = H^* f_{cc} (T_c - T_e) + h_c M_{cc}$	(23)
	$Q_J = \frac{\mathbf{j} \cdot \mathbf{j}}{\sigma_{mix}} + \frac{\mathbf{J} \cdot \mathbf{J}}{\sigma}$	(24)
Heterogeneous Nucleation	$N_{nu} = \frac{D(\Delta T)}{Dt} \cdot \frac{n_{max}}{\sqrt{2\pi\Delta T_\sigma}} e^{-\frac{1}{2}(\frac{\Delta T - \Delta T_N}{\Delta T_\sigma})^2}$ with $\frac{D(\Delta T)}{Dt} = \frac{\partial(\Delta T)}{\partial t} + m\mathbf{v}_l \cdot \nabla c_l - \mathbf{v}_l \cdot \nabla T_l$	(25)
Columnar Fragmentation	$N_{frag} = \frac{M_{cc}}{\tilde{\rho} \rho (\lambda_{2/c})^3}$	(26)

Neighboring cells will be marked as columnar tips. And the columnar growing direction will be determined according to the temperature gradient. The columnar growing direction is recorded and tracked by a unit vector in each control cell. A detailed description of the mass transfer rates and the tracking of the columnar growing direction are described in the authors' previous

study,^[15] in which the model was validated by comparing temperature fields, solute segregation, macrostructure, and the columnar growing direction with experimental results.^[16] Key modifications and features of the current model are described as follows.

- (1) The three Eulerian phases (liquid melt, equiaxed grains, and columnar crystals) are assumed with the

same density. A correction density is used to calculate the thermosolutal convection and equiaxed grain sedimentation. Solidification shrinkage and thermal shrinkage are ignored.

- (2) Control cells are marked with an index to distinguish liquid bulk, columnar front, and columnar trunk. The columnar front grows from mold walls perpendicularly. The growth velocity and radius of columnar tips are determined by the Lipton-Glicksman-Kurz (LGK) model.^[24] When a cell is first marked as the columnar front, the columnar growing direction is recorded according to the greatest undercooling gradient.
- (3) An equiaxed grain packing method^[25] is implemented to model the rigid structure. Columnar crystals and rigid structures move at a predefined velocity, obtained by solving single-phase Navier-Stokes equations with an infinite solid viscosity^[26] based on the casting speed and the mold shape. Subsequently, cell indexes for columnar and rigid structures, the average length of columnar tips, and the columnar growing direction are tracked based on the predefined velocity.
- (4) The heterogeneous nucleation theory^[27] and the columnar fragmentation model,^[28] which is based on the flow-enhanced remelting of dendrites, are used to calculate the formation of the active nucleus. The capillary-driven fragmentation model proposed by Rodrigues *et al.*^[29] is not considered in the present model.
- (5) A concept of envelope scheme is used to treat the morphology of equiaxed grains and columnar crystals. The interdendritic melt within the envelope is simplified as a part of solid dendrites. Mass transfer rates due to solidification and melting are calculated by the diffusion-governed growth kinetic.^[30] Species back diffusion in the solid phase is considered, although the impact of this term is very small.
- (6) The Kozeny-Carmen empirical correlation ($K_{K\&C} = \frac{\lambda^2(1-f_c)}{4\tau^2 k_{K\&C} f_c^2}$) is used to describe the permeability of directional columnar structures. The constant $k_{K\&C}$ is assumed to be 9 in the normal direction of primary columnar crystals and 3 in the parallel direction.^[31] The anisotropic permeability tensor \mathbf{K}_c can be derived from the local permeability tensor of the directional columnar structure by coordinate transformation.^[32] The drag coefficient K_{le} between equiaxed and liquid phases is calculated using the model proposed by Wang *et al.*^[33]

The quantity with the subscript mix represents a volume-averaged value. For example, macrosegregation is characterized by mixed concentration $c_{mix} = f_l c_l + f_e c_e + f_c c_c$. A mixed electrical conductivity $\sigma_{mix} = f_l \sigma_l + f_e \sigma_e + f_c \sigma_c$ is used in the electric potential method. When calculating the external magnetic fields induced by EMBr and SEMs, the liquid electrical conductivity σ is used. The correction density for calculating the buoyancy force in liquid phase is $\tilde{\rho}_l = \rho_{ref}[1 + \beta_T(T_{ref} - T_l) + \beta_c(c_{ref} - c_l)]$, and the correction density for predicting the sedimentation of equiaxed grains is $\tilde{\rho}_e = \rho_s$.

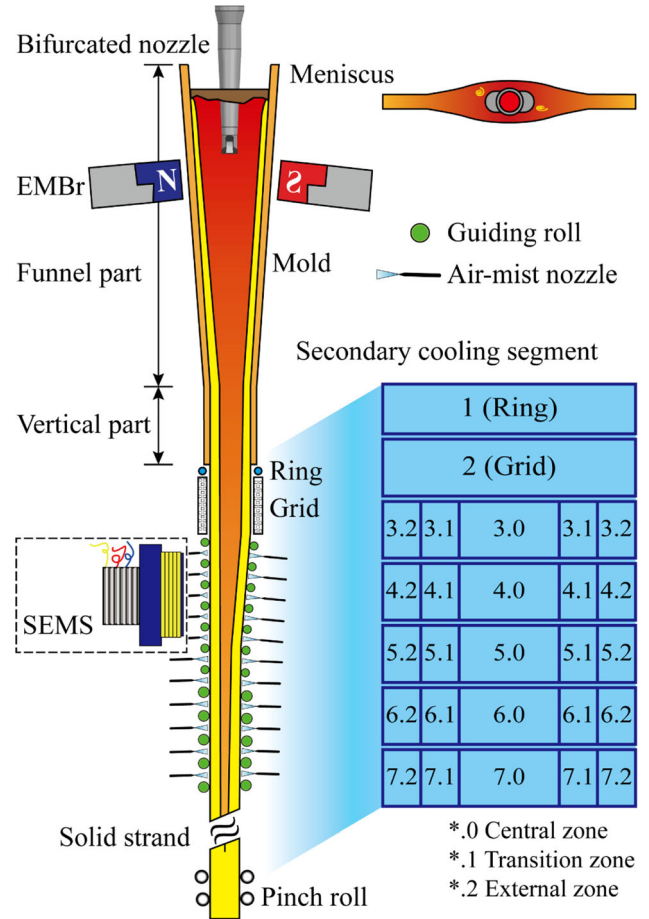


Fig. 1—Schematic diagram of the thin slab continuous casting (TSCC).

B. Physical Model

A schematic diagram of the TSCC is illustrated in Figure 1. A single-ruler EMBr is positioned just below the bifurcated submerged entry nozzle. The funnel-type mold is followed by a ring of water-spray nozzles, a heavy metallic grid, and SEMs which is on the fixed side. The secondary cooling system is divided into 17 loops to control water flow rates from spray and air-mist nozzles flexibly. No nozzles are arranged on narrow faces except at the spraying ring. The width of the secondary cooling system is 1.5 m, where the lengths of the central, transition, and external zones are 0.795 m, 0.355 m, and 0.35 m, respectively. Water flow rates in the mold and at different control loops are listed in Table II, which are used for calculating heat flux boundary conditions. It should be noted that a liquid core reduction technology can be applied in the studied CSP process. In the present work, the technology was not considered in the model.

The cross-section of the continuous casting slab from the mold outlet is 1250 mm × 85 mm. In Figure 2(a), the calculation domain is divided into hexahedral cells. The yellow line represents the cells at the outermost layer of the free surface, which are marked as columnar fronts. Columnar crystals are assumed to grow from mold walls perpendicularly. Heat flux boundary conditions are

Table II. Water Flow Rates in the Continuous Casting Process

Zone	Identification	Length (m)	Water Flow Rate (L/Min)
Mold	wide face	1	6500
	narrow face		200
Ring	wide face	0.06	300
	narrow face	0.319	
Grid	2	0.49	1964
Seg.1	3.0	1.27	884
	3.1		392
	3.2		392
Seg.2	4.0	1.975	777
	4.1		518
	4.2		518
Seg.3	5.0	1.83	457
	5.1		305
	5.2		305
Seg.4	6.0	1.84	336
	6.1		224
	6.2		224
Seg.5	7.0	1.84	141
	7.1		94
	7.2		94

applied on wide and narrow faces using the expressions proposed by Petrus *et al.*^[34] In this work, average heat flux is applied by ignoring the distribution of spray or air-mist nozzles and guiding rolls. The predefined columnar velocity is obtained by solving single-phase Navier-Stokes equations based on the casting speed U_{cast} .^[26] The boundary velocity on mold walls is:

$$\mathbf{v}_{\text{wall}} = U_{\text{cast}} \cdot \frac{\mathbf{n}_z - (\mathbf{n}_z \cdot \mathbf{n}_f) \cdot \mathbf{n}_f}{|\mathbf{n}_z - (\mathbf{n}_z \cdot \mathbf{n}_f) \cdot \mathbf{n}_f|} \quad [27]$$

The cross-section of the EMBr iron core is 200 mm high and 1200 mm wide. The distance between the surface of the iron core and the mid-section of wide faces is 150 mm. The center of the iron core is 415 mm below the meniscus. A schematic diagram of the SEMS is shown in Figure 2(b). The SEMS is positioned on the fixed side of the strand. The magnet center is 1.9 m below the meniscus. The casting silicon steel is simplified as a binary alloy with a nominal silicon concentration of 2.1 wt pct. Its material properties, which are obtained from Thermo-Calc software using the TCFE7^[35] database, and operation parameters are listed in Table III.

The magnetic field is calculated by the ANSYS Mechanical APDL software using the harmonic method. Lorentz force and Joule heat generated from the SEMS and the static magnetic field induced by the EMBr are interpolated into the computational domain. Induced magnetic fields related to the turbulent melt flow are ignored due to a very low magnetic Reynolds number. The electromagnetic braking force is calculated using the electric potential method. The equiaxed-columnar solidification model is implemented in ANSYS Fluent (version 19.2) software. The SST $k-\omega$ mixture turbulence model is used to describe the transient melt flow.^[36] All conservation equations are solved sequentially using the Phase Coupled SIMPLE

scheme. Convection terms are discretized using the second-order upwind scheme. 30 iterations are adopted in each time step (0.02 s) to reduce the residual values of continuity, momentum, turbulence kinetic energy, specific dissipation rate, volume fraction, nucleation, and electric potential equations below the convergence limit of $1.0\text{e}-4$ and those of enthalpy and species conservation equations below $1.0\text{e}-6$. Microscopic evolution and exchange terms are calculated at each time sub-steps. Tracking the columnar and rigid structures is executed at the end of every time step. In the thin slab, the distribution of solidification variables in the thickness direction is more informative. The mesh length in the thickness direction is between 3 and 4 mm, which is fine enough to capture solidification variables. The length ratio in the width direction and the thickness direction is between 1 and 3. To save computing resources, the mesh in the casting direction is coarsened, except in the funnel mold region, as shown in Figure 2(b). The total number of hexahedral control volumes is 1.5 million. The grid number is verified by comparing the simulated shell thickness with the measurements from a breakout, which will be discussed below. One three-dimensional (3D) calculation takes about one month with 18 CPUs (Intel Xeon(R) Silver 4116, 2.10GHz) in parallel (Intel MPI).

III. MODEL VALIDATION

A. Validation of the Equiaxed-Columnar Solidification Model

To validate the equiaxed-columnar solidification model, a benchmark solidification experiment of the Sn-10 wt pct Pb alloy under the effect of natural convection is calculated.^[16] The 3D computational

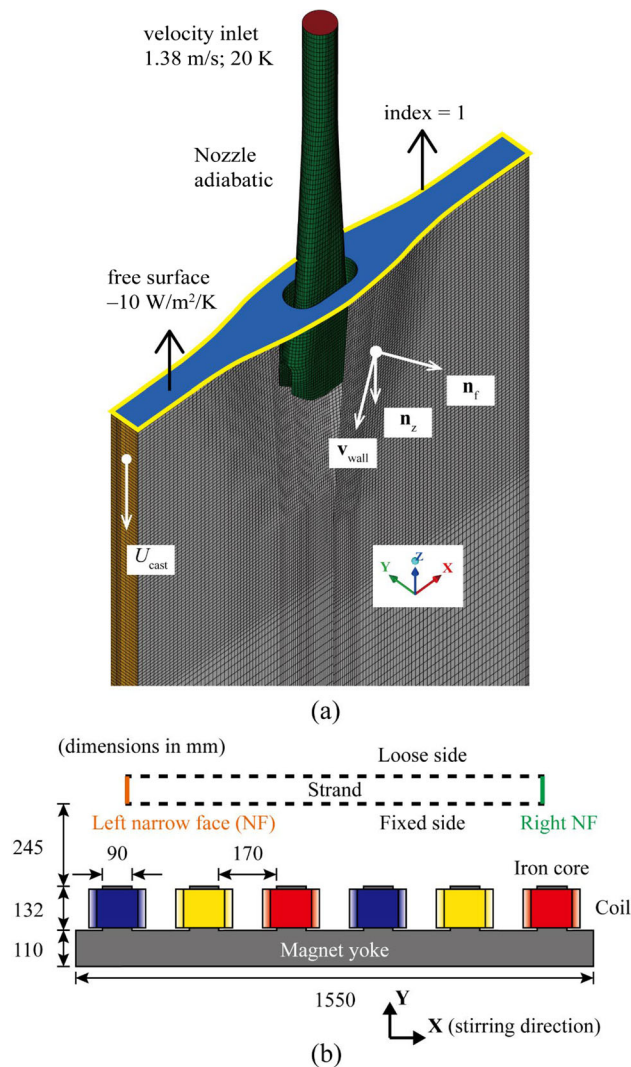


Fig. 2—(a) Boundary conditions in the mold region and (b) schematic diagram of the strand electromagnetic stirring (SEMS) in the top view.

domain and definite solution conditions are shown in Figure 3. The temperature difference between the two lateral walls is 40 K, with a 0.03 K/s cooling rate. All fluid boundary conditions are treated as no-slip walls. Material properties of the Sn-10 wt pct Pb alloy and the numerical procedure can be found in the previous work.^[15]

In Figure 4, simulation results are compared with experimental results, which are reprinted from the publication.^[16] The metallography of the experimental as-cast structure and the X-ray photo of the experimental solidified sample are displayed in Figures 4(b) and (d) respectively. The experimental equiaxed zone is enclosed by two white lines. The current solidification model predicts a similar equiaxed zone, which is mainly located in the upper-left region, extending to the middle bottom of the sample. An upwind tilted columnar structure

distributes in the right region, and the columnar growing direction is gradually sloping downwards as solidification proceeds. This trend can be evident from the distribution of the equiaxed phase outside the columnar-to-equiaxed transition (CET) line in the right region.

An isosurface for the mixed solute concentration greater than 0.14 is displayed in Figure 4(c). Positive macrosegregation is predicted in the ingot's lower-left part, accompanied with several short channels. Long segregated channels can be observed in the lower-right region. These phenomena are similar to the results in the X-ray photo of the experimental solidified sample, in which the light grey color corresponds to the lead-rich zone. It appears that the simulated channels near the lower-right corner are less and weaker than the experimental results. One important reason is that the temperature difference between the two lateral walls will decrease due to the contact resistance between the walls and sample surfaces. Other factors like thermal shrinkage and variable primary dendrite arm space can also affect the predicted chemical homogeneity. The primary dendrite arm space of Pb-Sn alloys is related to the temperature gradient, growth rate, and cooling rate,^[37] which is assumed to be constant in current work. However, the predicted distribution of equiaxed and columnar phases is close to the experimental as-cast structure. The key features of the macrosegregation and segregated channels are successfully predicted. These indicate that the current equiaxed-columnar solidification model is sufficiently reliable.

B. Validation of the Electrical Potential Method

To validate the electrical potential method implemented by the user-defined function in ANSYS Fluent, a simple case is performed according to the specific test problem and experimental measurements provided by Moreau.^[38] As shown in Figure 5, the calculated channel is 704 mm long and 40 mm high. A 304 mm long rectangular magnetic field is applied through the 2 mm thickness channel. The flow field under the influence of the rectangular magnetic field is calculated by a single-phase SST $k-\omega$ turbulence model coupled with the electrical potential method. The Lorentz force mainly appears at the edges of the magnetic field and opposes the flow. The Lorentz force is similar to the previous numerical results, which are calculated by Cukierski and Thomas^[39] using the FLUENT magnetohydrodynamics (MHD) module and standard $k-\epsilon$ turbulence model.

A quantitative comparison of the flow velocity along the vertical centerline of the channel is performed and shown in Figure 6. An “M-shaped” distribution is observed. Liquid metal in the channel tends to flow near the walls under the influence of the static magnetic field. The high velocity near the walls predicted by the present work is slightly higher than the experimental measurements and the previous simulation results. But the slope of the present velocity profile is closer to the

Table III. Material Properties of the Binary Fe–Si Alloy and Operation Parameters

Quantity	Symbol	Value (Unit)
Density	ρ	6880 (kg m ⁻³)
Solid Density	ρ_s	7190 (kg m ⁻³)
Thermal Conductivity	k_l, k_c, k_c	31 (W m ⁻¹ K ⁻¹)
Nominal Concentration	c_0	2.1 (wt pct)
Latent Heat	L	2.54e5 (J kg ⁻¹)
Viscosity	μ_l	0.006 (Pa s)
Specific Heat	c_p	750 (J kg ⁻¹ K ⁻¹)
Liquidus Slope	m	-1164 (K)
Liquidus Temperature	T_{liq}	1786 (K)
Solidus Temperature	T_{sol}	1773 (K)
Equilibrium Partition Coefficient	k_p	0.77 (-)
Thermal Expansion Coefficient	β_T	1.28e-5 (K ⁻¹)
Solute Expansion Coefficient	β_c	0.0074 (wt pct ⁻¹)
Primary Arm Spacing	λ_1	2e-4 (m)
Second Arm Spacing	λ_2	5e-5 (m)
Gibbs Thomson Coefficient	Γ	3e-7 (m K)
Diffusion Coefficient	$\frac{D_l}{D_c, D_c}$	1.34e-9 (m ² s ⁻¹) 3.0e-11 (m ² s ⁻¹)
Undercooling for Maximum equiaxed Nucleation Rate	ΔT_N	5.0 (K)
Gaussian Distribution Width	ΔT_σ	2.0 (K)
The Maximum Density of Grains	n_{max}	2e10 (-)
Fragmentation Coefficient	γ	3.0e-5 (-)
Electric Conductivity of Liquid Steel	σ	7.1e5 (S m ⁻¹)
Electric Conductivity of Liquid Steel	σ_e, σ_c	7.7e5 (S m ⁻¹)
Casting Speed	U_{cast}	4 (m min ⁻¹)
Superheat	ΔT_{cast}	10 (K)
EMBr Electric Current	I_{EMBr}	250 (A)
SEMS Electric Current	I_{SEMS}	600 (A)
SEMS Frequency	f_{SEMS}	3.5Hz
Windings Per Coil	N	100 (-)

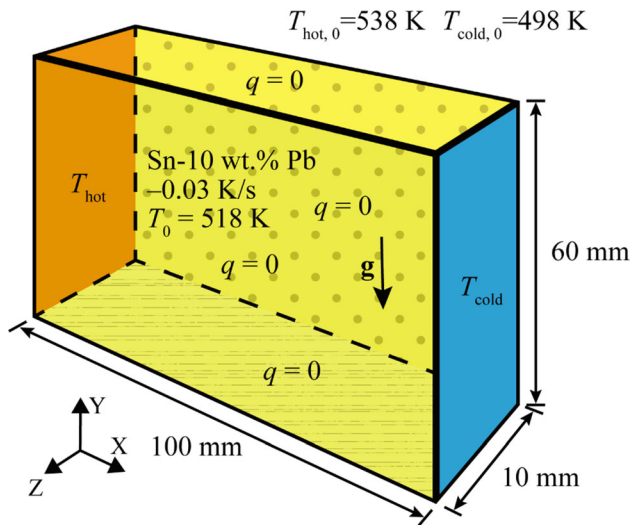


Fig. 3—The computational domain of the casting sample for validation.

measurements. It can be concluded that the prediction of the flow field under the effect of the applied electromagnetic field is accurate using the electrical potential method implemented by the user-defined function.

IV. RESULTS AND DISCUSSION

A. Physical Processes in the Whole Strand

Multi-physical fields in the middle section of the whole strand and the effects of the SEMs on the continuous casting process are discussed preliminarily. The velocity magnitude of the liquid steel is presented in Figure 7(a). Black lines represent the schematic flow pattern. The intensity of the nozzle jet can be suppressed visibly by EMBr, and an asymmetry double-roll flow pattern forms when the SEMs is off. The intensity of the lower roll is stronger than that of the upper roll because of the downward angle of the nozzle outlets. The flow pattern is significantly altered after the application of the SEMs. The one-way moving magnetic fields drive the liquid steel towards the right narrow face, which is in the stirring direction. Two vertical recirculation regions emerge after the liquid steel impinges on the right narrow face. The upper recirculating flow deflects nozzle jets and assembles the nozzle jet into a single stream, which is subsequently stirred by the SEMs and impinges towards the right narrow face. The lower recirculation makes liquid steel impinge into the liquid core more deeply, especially in the stirring direction.

It can be speculated that the vertical recirculating flow pattern is beneficial to increasing the residence time of liquid steel in the strand. As shown in Figure 7(b), the distribution of the constitutional undercooling provides

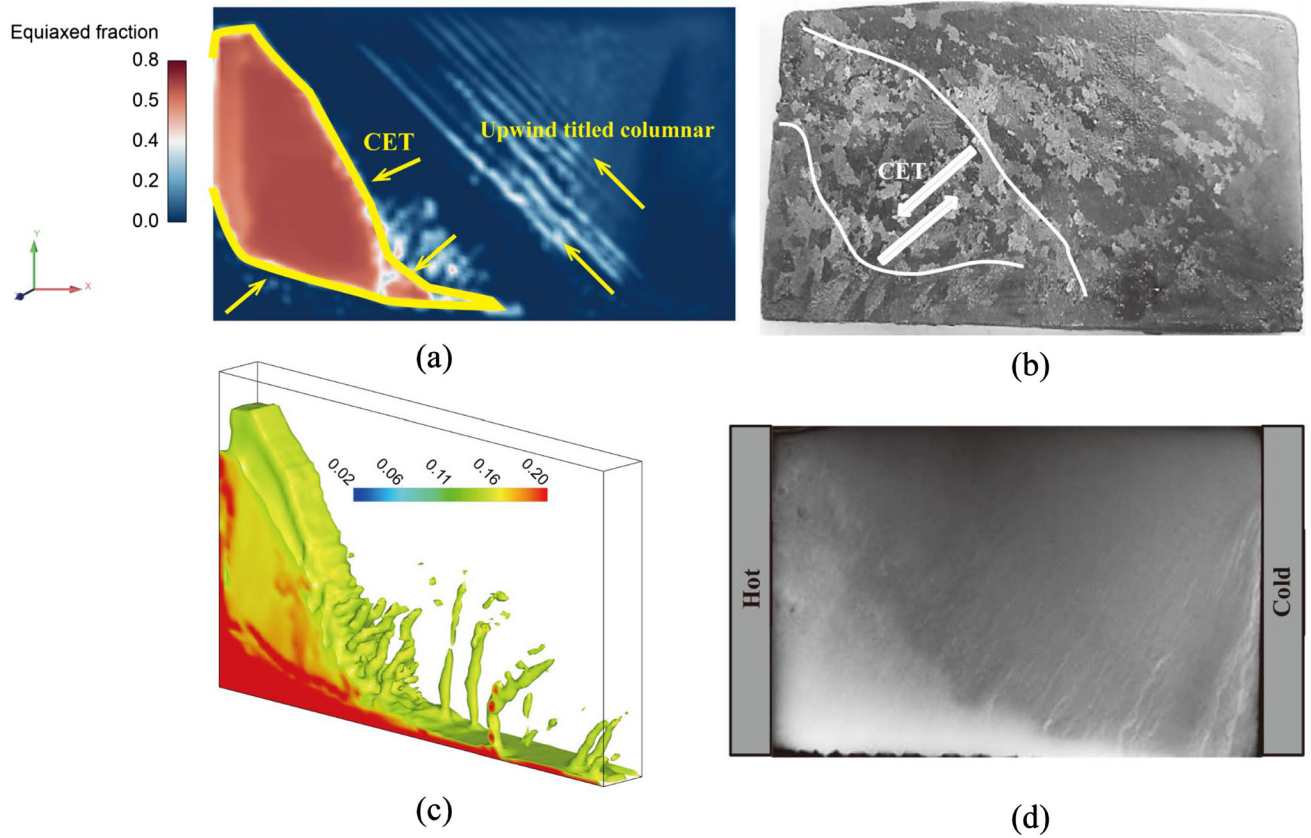


Fig. 4—Comparison of simulation results with the experimental sample: (a) simulated equiaxed volume fraction in the middle cross-section, (b) metallography of the experimental as-cast structure, (c) three-dimensional view of the isosurface of $c [\text{Pb}] > 0.14$, and (d) X-ray photo of the experimental solidified sample. The light grey color in (d) corresponds to the lead-rich zone. (b) and (d) are reprinted from publication^[16] (Color figure online).

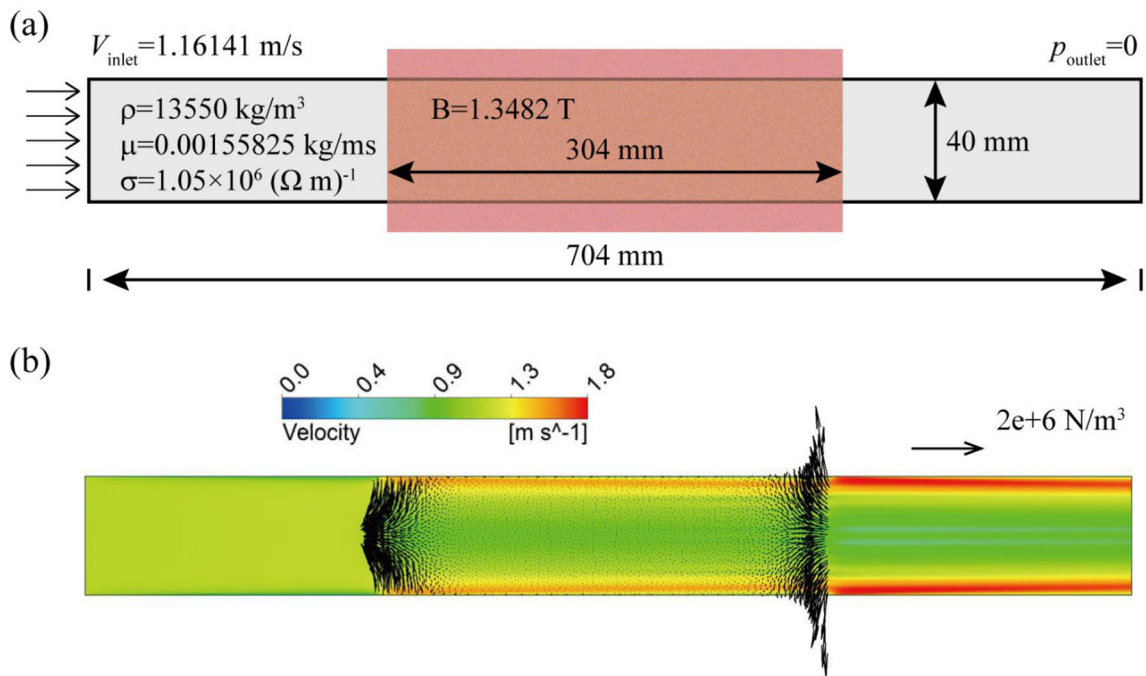


Fig. 5—Calculated channel (a) and simulation results (b). The velocity contour and Lorentz force are obtained in the steady state of the flow field. The channel length is scaled by 0.5 times.

a visual description of the flow pattern. The steel temperature is below the liquidus temperature in the cores of the lower rolls and the two vertical recirculation regions. When the SEMS is on, a deeper position of the liquidus line can be found in the stirring direction, and the area below the liquidus temperature looks smaller. The distribution of constitutional undercooling is changed obviously. Moreover, the two undercooled

recirculation regions are separated by a superheated melt region, which is assembled by the SEMS and impinges towards the right narrow face.

Equiaxed and columnar phases will remelt when the constitutional undercooling is negative. A positive constitutional undercooling indicates that the nucleus can be activated. The equiaxed volume fraction and heterogeneous nucleation rate on the middle plane of wide faces of the whole strand are displayed in Figures 7(c) and (d), respectively. A small equiaxed fraction can be found in the core of the upper recirculation region after the application of SEMS. This is not observed obviously in the core of lower rolls without SEMS though the constitutional undercooling is positive and heterogeneous nucleation occurs. One main reason is that the flow field is unsteady, and equiaxed grains will remelt once they are transported into the negative constitutional undercooling zone. The upper and lower recirculating flows are relatively stable for the formation and survival of equiaxed grains when the SEMS is on. In addition, more equiaxed grains can be found at the end of solidification, *i.e.*, in the center of the casting strand. It should be noted that the nucleus generated from columnar fragmentation is not displayed here because the nucleation rate is comparatively insignificant in comparison to the undercooling nucleation rate. Although the SEMS can enhance columnar fragmentation in the strand, this improvement can be ignored for increasing ECR. A possible explanation for this is that the continuous casting silicon steel has little difference between the liquidus and solidus lines. Silicon steel can solidify rapidly and the flow in the mushy zone is weak. What is more, the fragmentation coefficient

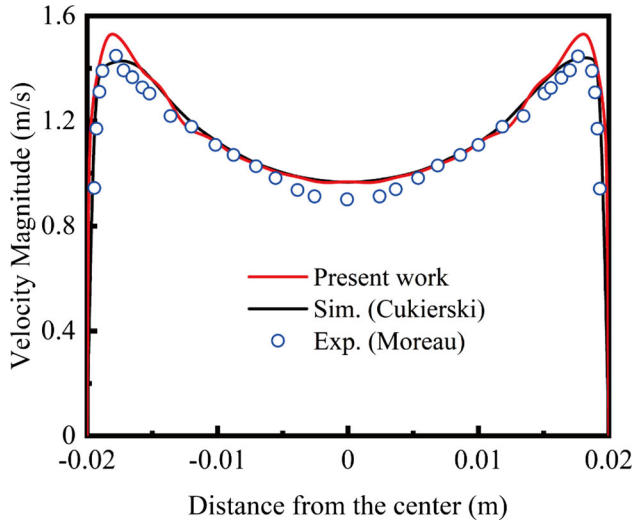


Fig. 6—Quantitative comparison of the flow velocity along the vertical centerline of the channel.

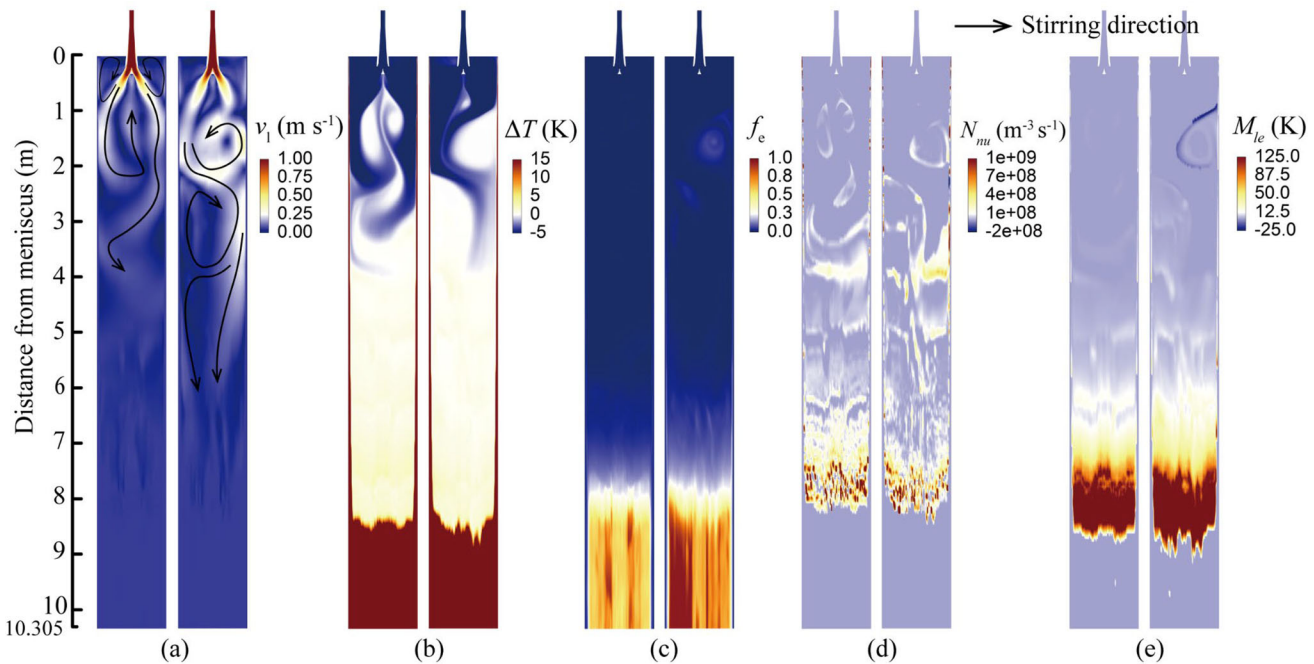


Fig. 7—Effects of SEMS on the whole solidification process: (a) the velocity magnitude, (b) constitutional undercooling, (c) equiaxed volume fraction, (d) heterogeneous nucleation rate, and (e) the mass transfer rate from liquid steel to equiaxed grains. Multi-physical fields on the right side of the five compared results are calculated after applying SEMS.

should be determined experimentally. The effect of the SEMS on undercooling nucleation is discussed in the following section.

The mass transfer rate from liquid steel to equiaxed grains is shown in Figure 7(e). The remelting of equiaxed grains can be observed obviously at the edge of the upper recirculation region. When the SEMS is on, the position of the solidification end is further away from the meniscus. According to Figure 7(b), the

metallurgical length becomes longer after applying the SEMS, especially in the stirring direction. Overall, these results indicate that the one-way moving magnetic field generates two recirculation regions in the strand, which are separated by a superheated melt. The transport of superheat and the nucleation processes are remarkably changed after applying the SEMS.

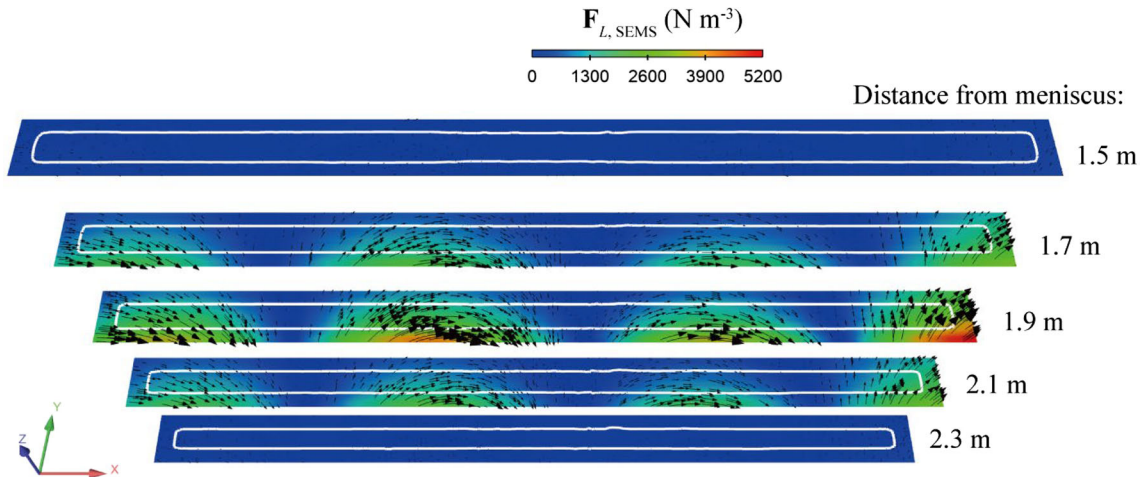


Fig. 8—The magnitude of the Lorentz force on the cross-sections at different distances from the meniscus. On each cross-section, the vector represents the tangential direction of the force, and the white curve indicates the position of the solidification front.

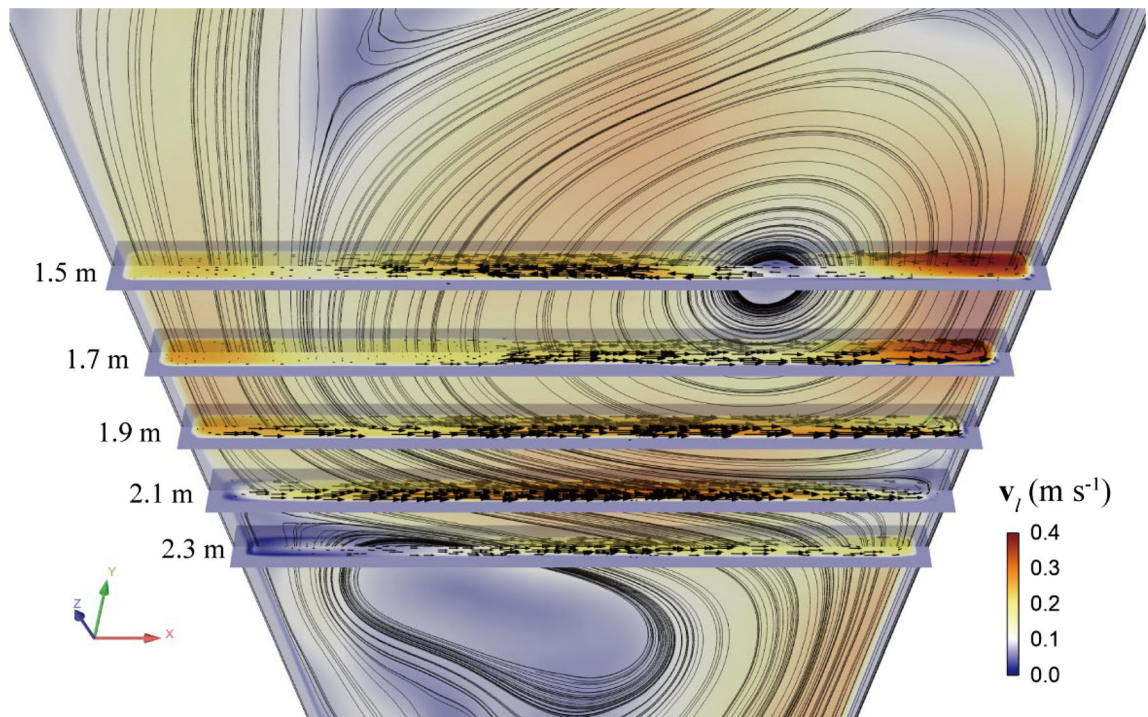


Fig. 9—Velocity distribution of liquid steel under SEMS. The black curve on the middle plane is the streamline of the liquid phase. The vectors represent the liquid steel flow direction on each cross-section.

B. Effects of SEMS on the Flow Field

The Lorentz force on different strand cross-sections is shown in Figure 8. The top edge of the stirrer iron core is 1.7 m from the meniscus, and the bottom edge is 2.1 m from the meniscus. Figure 8 presents the Lorentz force is mainly distributed in the area of the iron core. In the thickness direction, the electromagnetic force is mainly distributed on the fixed side, *i.e.*, the SEMS equipment side. White curves in each cross-section represent the position of the columnar front, indicating that the Lorentz force mainly acts on the solidified shell. It can be inferred that the stirring effect on the liquid steel will be weaker if the position of the stirrer equipment is further away from the meniscus. After statistics, the proportions of average electromagnetic force in the solidified shell area are 0.58, 0.6, and 0.64 on the three cross-sections of 1.7 m, 1.9 m, and 2.1 m from the meniscus, respectively. It is evident that the effect of electromagnetic stirring on the molten steel in the liquid cavity gradually weakens with the advancement of the solidification front.

The results in Figure 7(a) show that the nozzle jet will be affected by the upper recirculating flow and assembles one stream of superheat melt, forming relatively stable upper and lower recirculation regions under the one-way moving magnetic field. Figure 9 displays the liquid flow behavior near the stirrer equipment in more detail. In the middle plane of wide faces, the upper and lower recirculation centers are located on both sides of

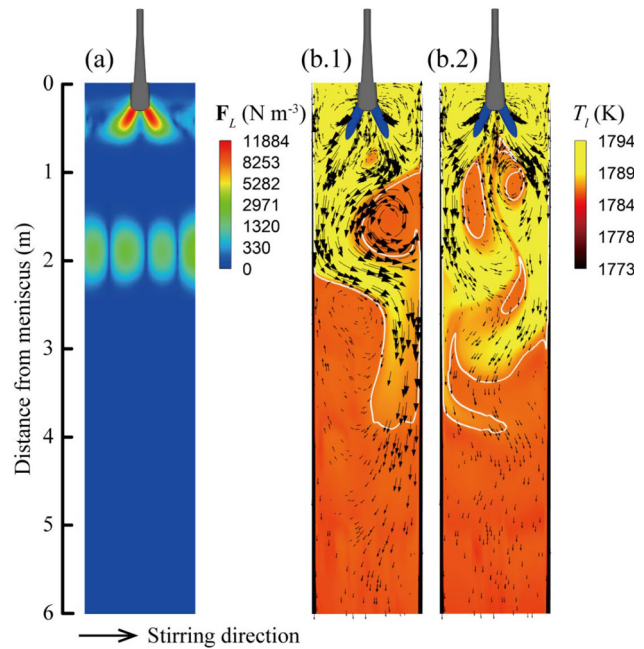


Fig. 11—(a) Lorentz force in the middle plane of wide faces. The effect of the SEMS on temperature distribution (b.1) compares to the case when no electromagnetic stirring is applied (b.2). The blue surfaces represent the isosurface with a liquid velocity equal to 0.4 m/s. The white lines represent the liquidus line (Color figure online).

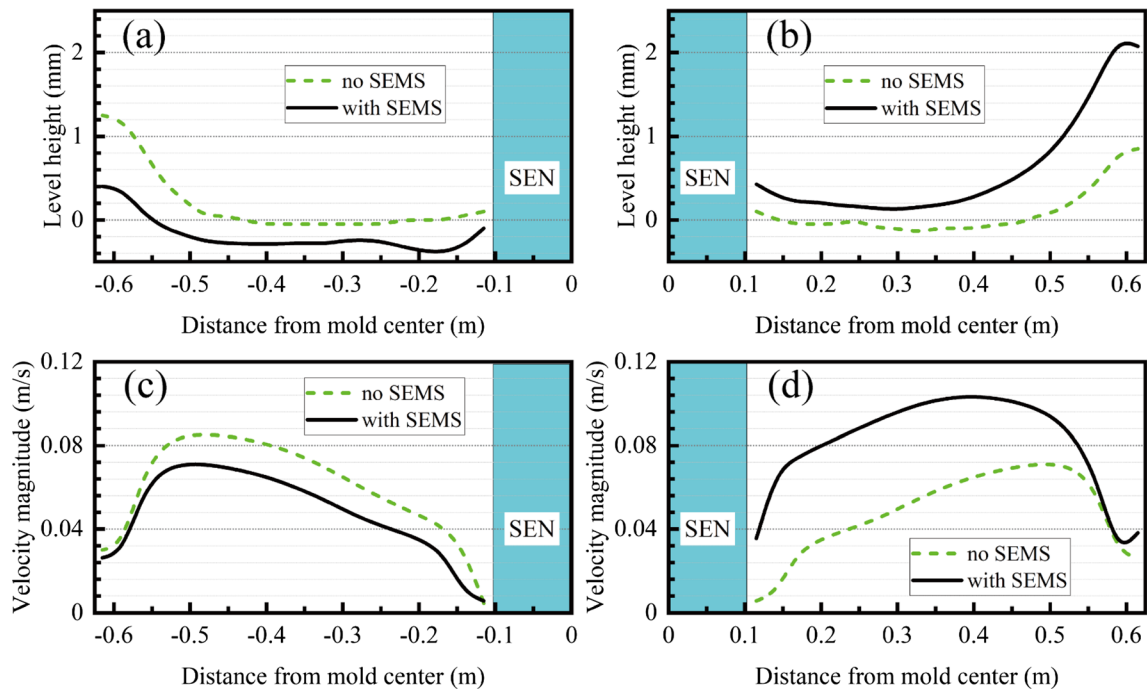


Fig. 10—Effect of SEMS on the level height and velocity magnitude of the slag-melt interface. (a) Level height on the opposite side of the stirring direction, (b) level height in the stirring direction, (c) velocity magnitude on the opposite side of the stirring direction, and (d) velocity magnitude in the stirring direction.

the stirrer equipment respectively. The upward velocity is greater and promotes the nozzle jet in the stirring direction to deflect to the other side. The vector arrows show the liquid steel flow direction on each cross-section. No significant rotational flow can be observed. A previous study found that SEMs induced rotating flow in the vertical plane of the width and casting directions in a slab continuous casting process.^[10] The results in Figure 9 indicate that the current SEMs mainly induces a rotating flow in the casting direction.

It can be speculated that the upward recirculation flow can cause unstable asymmetric flow on both sides of the submerged entry nozzle in the slag-melt interface. The effect of the SEMs on the velocity and level height of the slag-melt interface is displayed in Figure 10. The level height is calculated according to the following equation:

$$h = \frac{p - p_{ave}}{(\rho - \rho_{slag})|g|} \quad [28]$$

where p is the static pressure at the monitor location, p_{ave} is the spatial-averaged pressure across the whole slag-melt interface, ρ is the liquid steel density, and ρ_{slag} is the slag density, which is assumed as 2800 kg m^{-3} in this study. The level height and velocity magnitude on both sides of the submerged entry nozzle is symmetrically distributed when SEMs is not applied. The velocity and level height near narrow faces are greater on account of the double-roll flow pattern in the mold. When the SEMs is on, the upward recirculation impacts the slag-melt interface in the stirring direction; consequently, the velocity and level height on this side increase. It appears that the one-way electromagnetic stirring force negatively affects the slag-melt interface, and surface quality will deteriorate if the stirring intensity is large enough. Another function of the EMBr is to reduce the harm of the upward recirculation to the slag-melt interface. An important question for future studies is to explore the possible synergy of EMBr and SEMs in the TSCC.

Lorentz force induced by the EMBr and SEMs in the middle plane of wide faces is displayed in Figure 11(a). The electromagnetic force induced by the EMBr is mainly distributed near the nozzle jet and can suppress the flow intensity effectively. In Figure 11(b), the 0.4 m/s velocity is represented by the blue isosurface. The electromagnetic stirring force is smaller than the braking force and points towards the right narrow face, as shown in Figure 8. Two recirculating flow regions come into being. The upward recirculating flow deflects the nozzle jet impinging towards the right narrow face and assembles one stream superheat melt, as discussed in Figure 7(b). Compared to the case without SEMs, the area where the liquid temperature is above the liquidus line decreases. According to Figure 7(a), the average equiaxed volume fraction in the upper recirculation region is about 0.1, where the temperature is below the liquidus line. Equiaxed grains will rotate in this region due to the drag force between liquid and equiaxed phases. Due to the solid density greater than liquid steel, equiaxed grains in this region will finally sink through

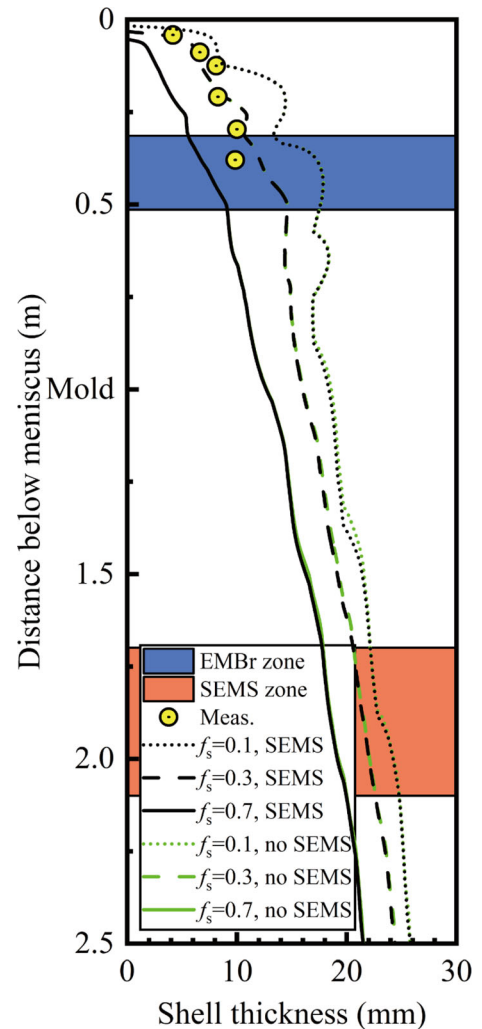


Fig. 12—Solidified shell thickness along the center of the wide face of the fixed side.

the superheat melt region. Part of equiaxed grains remelts when they encounter the jet flow with the high temperature outside the recirculation region, as shown in Figure 7(e). Without SEMs, an asymmetrical under-cooled region can also be observed out of the mold, appearing in the centers of the down-rolls. The position that favors the formation and growth of equiaxed grains appears later. SEMs will facilitate the emergence of this position earlier. The influence of the SEMs on solidification and equiaxed grain formation will be introduced in detail in the next section.

C. Effects of SEMs on the Solidification Process

Solidified shell thickness along the wide face of the fixed side is displayed in Figure 12. The breakout measurements from a thin slab continuous casting process^[40] are used to validate the current solidification model. The casting speed was 4.3 m/min in the process. Although the current operating parameters are not the same as that performed in the experimental measurements, these measurements are valuable for indirectly

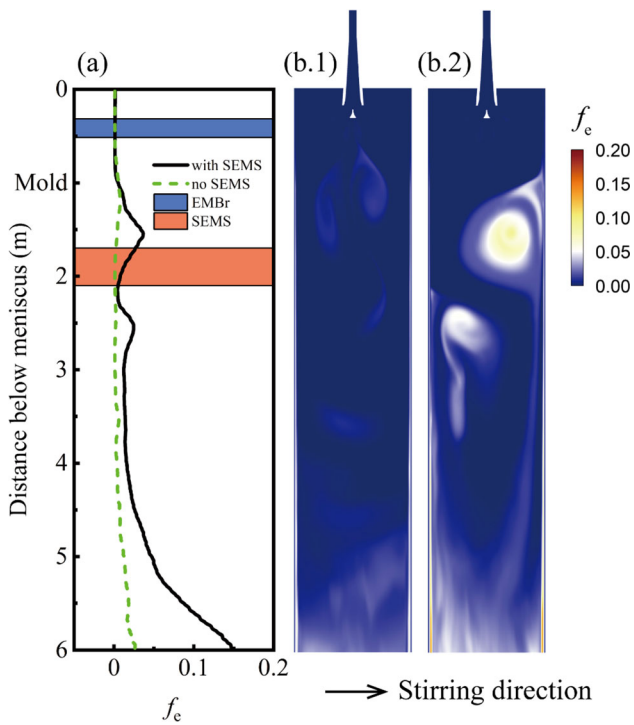


Fig. 13—Effect of SEMs on the formation and transportation of the equiaxed phase: (a) the evolution of the equiaxed volume fraction on the outside of the columnar solidification front, and the equiaxed volume fraction in the middle plane of wide faces without SEMs (b.1) and with SEMs (b.2).

validating numerical solidification models. Figure 12 shows that the columnar fraction equal to 0.3 shows a good agreement with the measurements. It should be clarified that the operation delay and partial solidification after the breakout should be considered. During the initial solidification, both numerical and experimental solidified shell thicknesses increase rapidly, indicating a high initial solidification rate. The fluctuation of solidified shell thickness can also be observed in simulation results, especially from the numerical result of $f_c = 0.1$. Consequently, the evolution of the shell thickness can be well-tracked using the present volume-averaged solidification model.

The solidified shell thickness becomes thinner after applying SEMs although the difference is not significant. This feature is more obvious in the numerical result of $f_c = 0.1$, especially above the SEMs zone. According to Figures 7(a) and 9, the liquid velocity in the upper recirculation region increases under the action of electromagnetic stirring. One important reason causing this minor difference is the casting material property. The difference between the liquidus and solidus lines of silicon steel is small, and the solute equilibrium partition coefficient is close to 1. Silicon steel will quickly solidify in the continuous casting process, causing a thin mushy zone. The rejected solute is not significantly affected by the flow field.

To deeply study the function of the SEMs, the variation of physical quantities on the outside of the columnar solidification front with the distance from the meniscus is analyzed. Figure 13(a) displays the

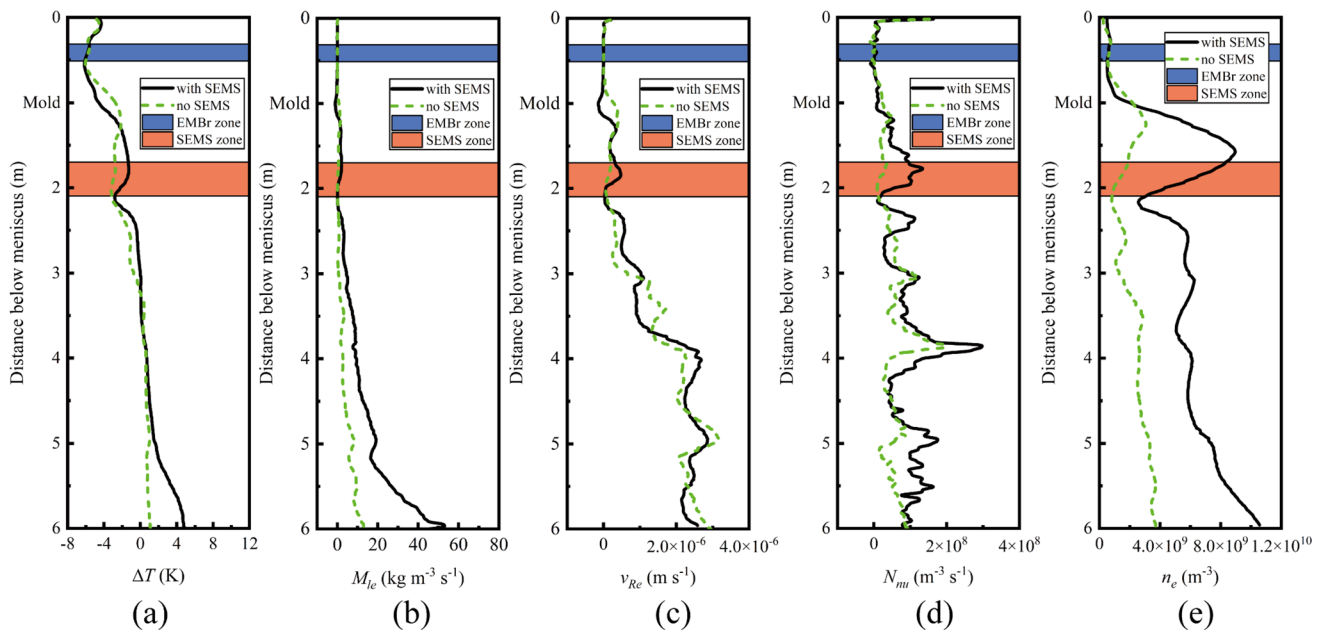


Fig. 14—Solidification quantities in the liquid pool with the distance from the meniscus: (a) undercooling, (b) mass transfer rate from the liquid steel to equiaxed grains, (c) growth speed in the radius direction of equiaxed grains, (d) heterogeneous undercooling nucleation rate, and (e) the nucleus number density.

formation and transportation of the equiaxed phase. The average equiaxed volume fraction increases flatly with distance to the meniscus without SEMs. When the SEMs is on, the average equiaxed volume fraction increases rapidly after 5 m from the meniscus. Two curve peaks can be found on the upper and lower sides of the SEMs zone, which correspond to the upper and lower recirculation regions. Equiaxed grains will remelt in the SEMs zone, *i.e.*, the superheat melt region, which can be seen in Figure 11. Figures 13(b.1) and (b.2) display the corresponding equiaxed volume fraction in the middle plane of wide faces. It appears that electromagnetic stirring has a significant effect on the transport of the equiaxed phase. The reason for this interesting phenomenon needs more analysis of the solidification quantities in the liquid pool.

Figure 14(a) shows the average undercooling in the liquid pool with the distance from the meniscus. The undercooling decreases gradually in the beginning because of the nozzle jet and then increases with the distance from the meniscus. When the SEMs is on, the classical double-roll flow pattern is changed to the upper and lower recirculating flow, separated by a gathered superheat melt near the stirring zone. Thus, the average undercooling will decrease again in the SEMs zone, as shown by the black line in the figure. Superheat is redistributed and the temperature gradient in the liquid pool becomes more uniform. The undercooling in the upper recirculation region becomes higher because the residence time of the liquid steel in this region increases. After 5 m from the meniscus, there is a steep rise in the undercooling when the SEMs is on.

The mass transfer rate from the liquid steel to the equiaxed phase increases markedly after 5 m from the meniscus, as shown in Figure 14(b). According to the Eq. [11], the growth speed in the radius direction of equiaxed grains and the grain size are the main factors determining the mass transfer rate. Since the current model assumes equiaxed grains as regular uniform spheres, the grain size is equivalent to the diameter of equiaxed grains, *i.e.*, the nucleus number density. The average growth speed in the radius direction of equiaxed grains is displayed in Figure 14(c). No significant differences between the two cases are observed. This indicates that the determined reason for improving the solidification rate of the equiaxed phase after applying SEMs is the nucleus density present in the liquid phase.

The heterogeneous undercooling nucleation rate and the nucleus number density are displayed in Figures 14(d) and (e) respectively. The nucleation rate is high during initial solidification and then sharply drops to zero. When the SEMs is on, the nucleation rate increases in the upper recirculation zone and decreases after the SEMs zone. The nucleation rate with electromagnetic stirring is generally higher than without electromagnetic stirring. According to Figure 14(e), the nucleus number density increases rapidly in the upper recirculation region and decreases in the SEMs zone, *i.e.*, the superheat melt region described above. From the upper recirculation region, the nucleus number density in the liquid pool is higher than when no electromagnetic stirring is applied. It is important to clarify that the contribution of columnar fragmentation to the increase in the nucleus number density is

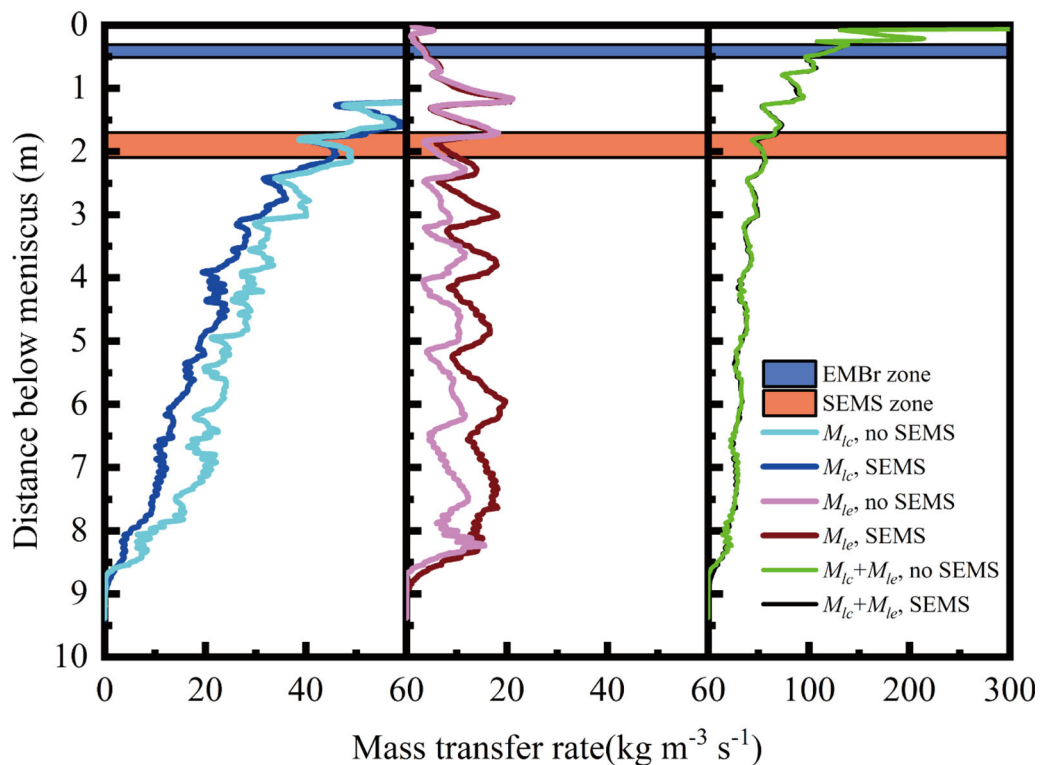


Fig. 15—Mass transfer rates from the liquid steel to columnar crystals (M_{lc}) and equiaxed grains (M_{le}).

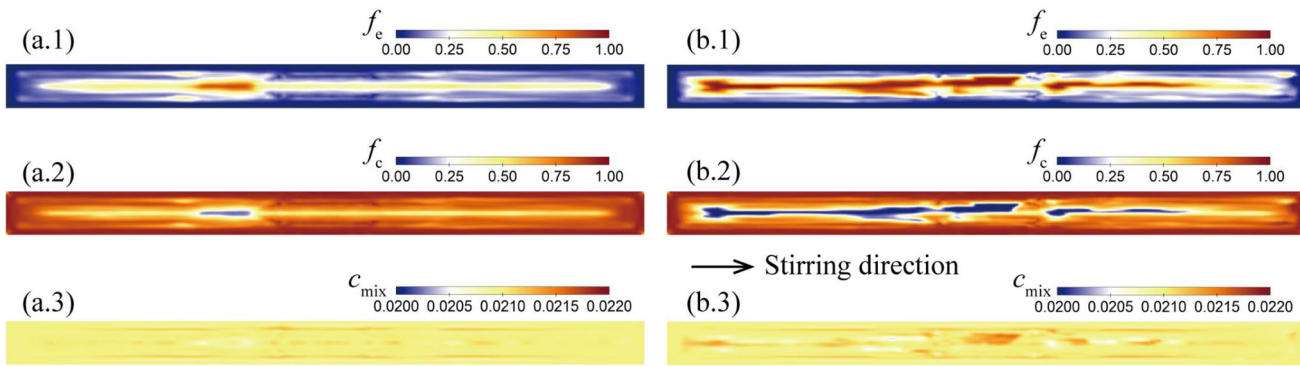


Fig. 16—The distribution of as-cast structure and macrosegregation in the final strand cross-section: (a) without SEMS, and (b) with SEMS. (a.1) and (b.1): the equiaxed phase volume fraction; (a.2) and (b.2): the columnar phase volume fraction; (a.3) and (b.3): the mixed solute concentration.

comparatively insignificant. One important reason is that the continuous casting silicon steel has little difference between the liquidus and solidus lines. The liquid flow in the mushy zone is weak due to the rapid solidification of silicon steel. Another reason is that the solute equilibrium partition coefficient of silicon steel is close to 1, indicating that the rejected solute concentration in solid columnar dendrites is difficult to melt dendrite arms and form equiaxed grain nucleus. Overall, the gradual accumulation of crystal nuclei is crucial in promoting the mass transfer from liquid steel to the equiaxed phase.

Mass transfer rates from the liquid steel to equiaxed grains and columnar crystals on the entire strand cross-section throughout the continuous casting process are compared in Figure 15. At the initial solidification, liquid steel solidifies rapidly as the columnar structure. As the solidification proceeds, M_{lc} decreases gradually, while M_{le} is maintained almost within a certain range. Comparing to the case without electromagnetic stirring, the distribution of the total mass transfer rate to columnar crystals and equiaxed grains changes. M_{lc} is suppressed after the SEMS zone and M_{le} is improved. The total solidification rate ($M_{lc} + M_{le}$) is nearly unchanged before and after applying electromagnetic stirring. Furthermore, the solidification end is slightly shifted backward after the application of the SEMS, approximately by 10mm. This is because the electromagnetic stirring equipment generates Joule heat in the strand, and the additional heat source causes the completely solidified time to increase.

D. Effects of SEMS on Internal Quality

The effect of the SEMS on the final as-cast structure and macrosegregation is shown in Figure 16. The equiaxed phase mainly accumulates in the centerline of the strand. Almost no CET occurs when the SEMS is not applied. The columnar tip is tracked in the center of the strand. When the SEMS is applied, the equiaxed volume fraction visually increases, and the end of the columnar tip can be observed in Figure 16(b.2). Interestingly, the equiaxed volume fraction in the stirring direction is lower than that on the other side. This result

seems inconsistent with the results shown in Figure 13, in which more equiaxed grains can be observed in the upper recirculation region. Except for the equiaxed grains rotating in this region under the drag force between solid and liquid phases and remelt at the region edge, some grains settle through the superheat melt region and remelt under gravity. Furthermore, the gathered superheat melt impinges to the right narrow face and forms the downward recirculating flow, which leads to a later formation of equiaxed grains in the stirring direction. The ECR on the final cross-section of the strand is 4 pct in the absence of electromagnetic stirring, and it increases to 17.4 pct after applying the SEMS.

The macrosegregation is distributed appropriately, which should be between 0.02 and 0.022. This meets the quality needs of silicon steel products. The most likely reason is that the partition coefficient of the solute silicon in liquid steel is 0.77, indicating that the intensity of the solute redistribution is weak in the mushy zone. The macrosegregation is related to the distribution of the as-cast structure. Positive segregation can be found underneath the thin slab surface and in the equiaxed zone. Negative segregation can be found at the CET line. Compared to the as-cast structure, macrosegregation has limited potential for improving the solidification quality of thin slabs.

The current model predicts a low ECR although the SEMS is applied. There are three main reasons for this. First, the nucleation parameters predict less equiaxed nucleus in the solidification process. This results in a slower solidification rate for equiaxed crystals than for columnar crystals. Second, the columnar front advances too fast using the LGK model in view of the strong cooling intensity of thin-slab continuous casting. An empirical coefficient can be studied to modify the LGK model for a strong cooling condition. It is an indisputable fact that the application of the multiphase volume-averaged solidification model still requires a great deal of research. Compared to the conventional enthalpy-porosity model, the reliability of this model relies on more physical parameters. Third, the low ECR is related to many operating parameters, such as a weak stirring intensity, the strong cooling intensity of the

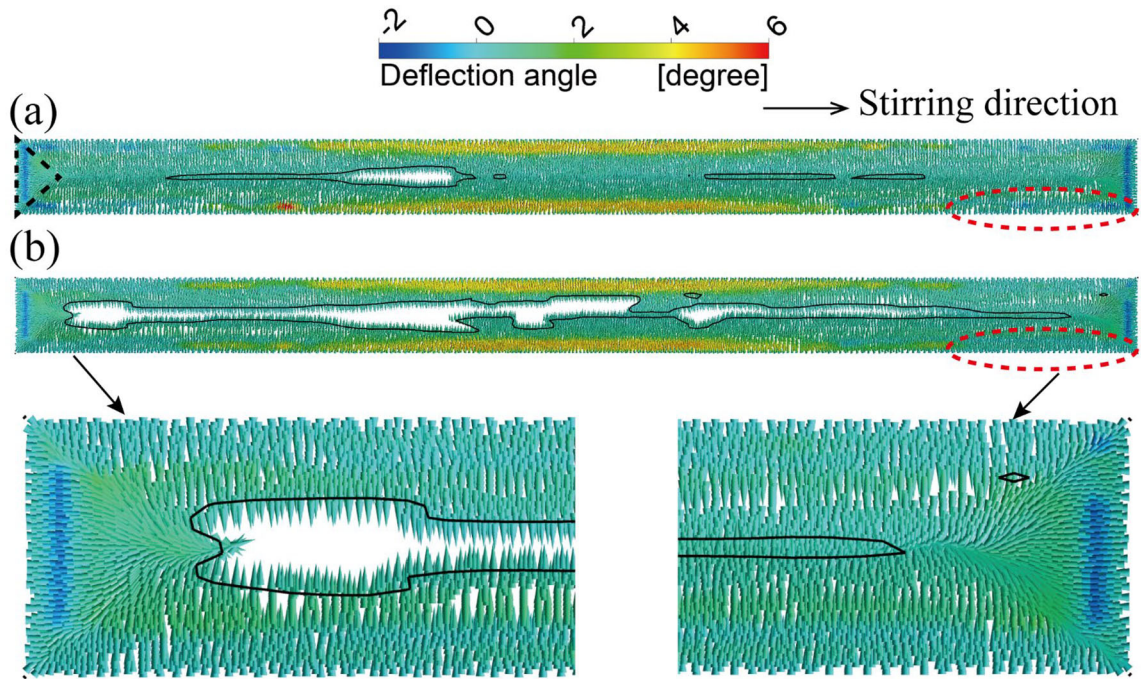


Fig. 17—Deflection angle in the casting direction of the casting steel: (a) with SEMS, (b) without SEMS. The black line represents the location $f_c = 0.5$.

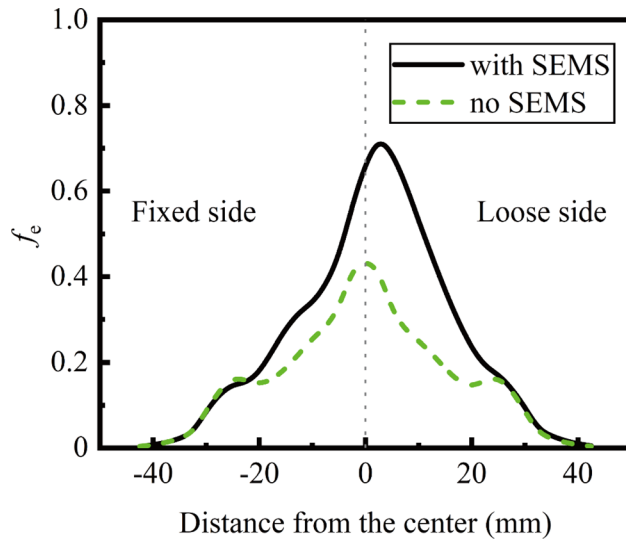


Fig. 18—Distribution of equiaxed volume fraction in the thickness of the final solidified strand.

secondary cooling zone, the steel grade, and unreasonable stirring modes. Further work is needed to validate the current model with industrial measurements and investigate a more reasonable stirring mode for a higher ECR.

The calculated columnar growing direction is compared in Figure 17. The black line represents the location $f_c = 0.5$. The columnar crystal area becomes smaller after the application of electromagnetic stirring. Columnar crystals grow from wide and narrow faces perpendicularly, forming triangle zones on the right and left narrow faces. The color of the vector arrows

represents the deflection angle of columnar crystals in the casting direction. On the side of the wide face, the deflection angle of columnar crystals is upward because the temperature gradient in the funnel-shaped mold is upward during initial solidification. In most cases, columnar dendrites grow horizontally. On the right and left sides, columnar crystals are deflected downward slightly. When the SEMS is applied, the deflection angle of columnar crystals growing from wide faces near narrow faces is more uniform, as marked by the red dashed lines in Figure 17. The maximum deflection angle is 4.7 deg, smaller than the case in the absence of SEMS, which is 7.3 deg. It can be inferred that the temperature gradient before the columnar front becomes more uniform when the liquid steel is stirred by the SEMS. It should be clarified that the calculated deflection angle in the present work is a volume-averaged deflection angle of primary columnar dendrites. The results are encouraging and should be validated by future in-plant experiments.

The distribution of the equiaxed volume fraction in the thickness direction of the final strand is displayed in Figure 18. Without electromagnetic stirring, the volume fraction is almost symmetrically distributed along the centerline of wide faces. The maximum fraction appears at the center with a value of 0.44. It should be noted that this value represents the average value over the entire width of the thin slab. When the SEMS is on, the maximum equiaxed fraction increases to 0.73. Interestingly, the peak location tends to appear on the loose side. This trend is a consequence of the rotating flow of liquid steel in the strand cross-section, though the effect of the SEMS on the horizontal flow is weaker than that on the casting direction. Equiaxed grains are more likely

to accumulate on the loose side under the influence of the rotating flow. Taken together, these results indicate that applying electromagnetic stirring is beneficial to the improvement of the ECR of the thin slab continuous casting. The effect of electromagnetic stirring on the ultimate distribution of equiaxed grains on the entire strand cross-section manifests in two aspects. First, the equiaxed volume fraction in the stirring direction is lower than the fraction on the other side. Second, equiaxed grains tend to accumulate on the loose side of the strand due to the rotating flow caused by the one-way moving magnetic field.

A limitation of the current volume-averaged solidification model is that the model does not predict fine-grained structures underneath the strand surface. The major reason is that columnar crystals are assumed to grow from wide and narrow walls directly. The columnar front can advance rapidly due to the high temperature gradient at initial solidification. To address this limitation in future work, the model should be improved to consider columnar crystals growing from the chill zone or rigid structure.

V. CONCLUSIONS

The present research aimed to demonstrate the effect of SEMs on the flow pattern, superheat transportation, macrosegregation, and as-cast structure in the thin slab continuous casting process. An improved equiaxed-columnar solidification model coupled with the electrical potential method was developed. The following conclusions were drawn.

- (1) The equiaxed-columnar solidification model was verified by a solidification benchmark experiment. The predicted as-cast structure and key features of the macrosegregation and segregated channels were consistent with the experimental results. The electrical potential method successfully predicted the flow field in the applied static magnetic field.
- (2) Two recirculating flow regions came into being under the one-way moving magnetic field induced by the SEMs. The upward recirculating flow deflected the nozzle jet and affected the balance of the slag-melt interface. Greater level velocity and level height were observed in the stirring direction.
- (3) A superheat melt was assembled by the SEMs and impinged towards the right narrow face, separating the two recirculation regions. Equiaxed grains settled from the upper recirculation region remelted in the superheat melt region. The downward recirculating flow led to a later formation of equiaxed grains. Finally, the equiaxed volume fraction in the stirring direction was lower than the fraction on the other side.
- (4) The application of SEMs was beneficial to the improvement of ECR. The ECR on the final cross-section of the strand was 4 pct in the absence of electromagnetic stirring, and it increased to 17.4 pct after applying the SEMs. The main reason was that the temperature gradient in the liquid pool be-

came flat, and more active nucleus formed and accumulated after the SEMs zone, accelerating the mass transfer rate from liquid steel to equiaxed grains.

This study has provided a deeper insight into the function of SEMs on the multiphase flow and as-cast structure in the thin slab continuous casting process using an equiaxed-columnar solidification model. A limitation of this model is that the fine-grained structure underneath the strand surface is not predicted. More broadly, laboratory or in-plant experiments are required to determine the modeling parameters and directly validate the equiaxed-columnar solidification model.

FUNDING

This work was supported by the National Natural Science Foundation of China (No. 51974071), National Key Research and Development Program of China (No. 2022YFB3705101), and the Opening project fund of Materials Service Safety Assessment Facilities (No. MSAF-2021-009).

CONFLICT OF INTEREST

The authors declare that they have no known competing financial interests or personal relationships that could have appeared to influence the work reported in this paper.

NOMENCLATURE

B	Magnetic flux density (T)
c_1, c_e, c_c	Species concentration (–)
c_{ref}	Reference concentration (–)
c_1^*, c_s^*	Equilibrium concentration at interface (–)
c_{mix}	Mixed concentration (–)
c_p	Specific heat ($J\ kg^{-1}\ K^{-1}$)
$C_{ij}(= -C_{ji})$	Species exchange term ($kg\ m^{-3}\ s^{-1}$)
D_1, D_e, D_c	Diffusion coefficient ($m^2\ s^{-1}$)
E	Electric field intensity ($V\ m^{-1}$)
f_1, f_e, f_c	Volume fraction (–)
$F_{ji}(= -F_{ij})$	Momentum exchange rate ($kg\ m^{-2}\ s^{-2}$)
F_L	Lorentz force ($kg\ m^{-2}\ s^{-2}$)
g	Gravity ($m\ s^{-2}$)
h_1, h_e, h_c	Enthalpy ($J\ kg^{-1}$)
H^*	Heat transfer coefficient between phases ($W\ m^{-3}\ K^{-1}$)
H	Magnetic field intensity ($A\ m^{-1}$)
j	Induced current density ($A\ m^{-2}$)
J	Current density ($A\ m^{-2}$)
k_1, k_e, k_c	Thermal conductivity ($W\ m^{-1}\ K^{-1}$)
$k_{K\&C}$	Kozeny–Carmen correlation constant (–)
$K_{K\&C}$	Mush permeability (m^2)
K_{lc}	Anisotropic permeability tensor (m^2)
K_{le}, K_{ce}	Drag force coefficient ($kg\ m^{-3}\ s^{-1}$)

L	Latent heat (J kg ⁻¹)
m	Liquidus line slope (K)
$M_{ji}(= -M_{ij})$	Mass transfer rate (kg m ⁻³ s ⁻¹)
n_e	Nucleus number density (m ⁻³)
n_{\max}	Maximum equiaxed grain density (m ⁻³)
\mathbf{n}_z	Unit vector in the casting direction (-)
\mathbf{n}_r	Unit vector in the slab surface (-)
N_{nu}	Heterogeneous undercooling nucleation rate (m ⁻³ s ⁻¹)
N_{frag}	Columnar fragmentation rate (m ⁻³ s ⁻¹)
p	Pressure (Pa)
$Q_{ji}(= -Q_{ij})$	Energy exchange term (W m ⁻³)
Q_j	Joule heat (W m ⁻³)
R_{tip}	Primary columnar tip radius (m)
S_c, S_e	Interfacial area concentration of envelope (m ⁻¹)
T_l, T_e, T_c	Temperature (K)
T_{ref}	Reference temperature (K)
ΔT	Constitutional undercooling (K)
ΔT_N	Undercooling for maximum nucleation rate (K)
ΔT_σ	Gaussian distribution width (K)
U_{cast}	Casting speed (m s ⁻¹)
$v_{c,\text{tip}}$	Growth speed of primary columnar tip (m s ⁻¹)
$\mathbf{v}_l, \mathbf{v}_e, \mathbf{v}_c, \mathbf{v}_{\text{wall}}$	Velocity vector (m s ⁻¹)
v_{Rc}	Growth speed in the radius direction of columnar trunks (m s ⁻¹)
v_{Re}	Growth speed in the radius direction of equiaxed grains (m s ⁻¹)
β_T	Thermal expansion coefficient (K ⁻¹)
β_c	Solutal expansion coefficient (-)
$\sigma, \sigma_e, \sigma_c$	Electrical conductivity (S m ⁻¹)
$\Phi_{\text{imp}}^c, \Phi_{\text{imp}}^e$	Growing surface impingement factor (-)
λ_1	Primary columnar arm space (m)
λ_2	Secondary columnar arm space (m)
μ_l	Viscosity (kg m ⁻¹ s ⁻¹)
μ_{mag}	Vacuum magnetic permeability (H m ⁻¹)
γ	Fragmentation coefficient (-)
ρ, ρ_s	Density (kg m ⁻³)
ρ_{ref}	Reference density (kg m ⁻³)
$\tilde{\rho}$	Correction density (kg m ⁻³)
φ	Electric potential (V)
τ_i	Stress-strain tensors (kg m ⁻¹ s ⁻¹)

SUBSCRIPTS

- c Columnar phase
- e Equiaxed phase
- l Liquid phase

REFERENCES

1. H. Yu, Y.L. Kang, K.L. Wang, J. Fu, Z.B. Wang, and D.L. Liu: *Mater. Sci. Eng. A*, 2003, vol. 363, pp. 86–92. [https://doi.org/10.1016/S0921-5093\(03\)00598-7](https://doi.org/10.1016/S0921-5093(03)00598-7).
2. P. Jayakrishna, S. Chakraborty, S. Ganguly, and P. Talukdar: *Can. Metall. Q.*, 2021, vol. 60, pp. 320–49. <https://doi.org/10.1080/00084433.2021.2014712>.

3. B.K. Li and F. Tsukihashi: *ISIJ Int.*, 2006, vol. 46, pp. 1833–38. <https://doi.org/10.2355/isijinternational.46.1833>.
4. R. Singh, B.G. Thomas, and S.P. Vanka: *Metall. Mater. Trans. B*, 2013, vol. 44B, pp. 1201–21. <https://doi.org/10.1007/s11663-013-9877-x>.
5. L.S. Zhang, X.F. Zhang, B. Wang, Q. Liu, and Z.G. Hu: *Metall. Mater. Trans. B*, 2014, vol. 45B, pp. 295–306. <https://doi.org/10.1007/s11663-013-9948-z>.
6. J. Sengupta, B.G. Thomas, H.J. Shin, G.G. Lee, and S.H. Kim: *Metall. Mater. Trans. A*, 2006, vol. 37A, pp. 1597–611. <https://doi.org/10.1007/s11661-006-0103-1>.
7. A. Vakhrushev, A. Kharicha, E. Karimi-Sibaki, M. Wu, A. Ludwig, G. Nitzl, Y. Tang, G. Hackl, J. Watzinger, and S. Eckert: *Metall. Mater. Trans. B*, 2021, vol. 52B, pp. 3193–3207. <https://doi.org/10.1007/s11663-021-02247-x>.
8. Z.Q. Liu, A. Vakhrushev, M.H. Wu, E. Karimi-Sibaki, A. Kharicha, A. Ludwig, and B.K. Li: *Metals*, 2018, vol. 8, p. 609. <https://doi.org/10.3390/met8080609>.
9. H. Shibata, S. Itoyama, Y. Kishimoto, S. Takeuchi, and H. Siekiguchi: *ISIJ Int.*, 2006, vol. 46, pp. 921–30. <https://doi.org/10.2355/isijinternational.46.921>.
10. J. Gong, H.P. Liu, X.H. Wang, and Y.P. Bao: *J. Iron. Steel Res. Int.*, 2015, vol. 22, pp. 414–22. [https://doi.org/10.1016/s1006-706x\(15\)30021-2](https://doi.org/10.1016/s1006-706x(15)30021-2).
11. C.J. Wang, Z.Q. Liu, and B.K. Li: *Metals*, 2021, vol. 11, p. 948. <https://doi.org/10.3390/met11060948>.
12. Z. Zhang, M.H. Wu, H.J. Zhang, S. Hahn, F. Wimmer, A. Ludwig, and A. Kharicha: *J. Mater. Process. Technol.*, 2022, vol. 301, p. 117434. <https://doi.org/10.1016/j.jmatprotec.2021.117434>.
13. T. Wang, L. Hachani, Y. Fautrelle, Y. Delannoy, E. Wang, X. Wang, and O. Budenkova: *Int. J. Heat Mass Transf.*, 2020, vol. 151, p. 119414. <https://doi.org/10.1016/j.ijheatmasstransfer.2020.119414>.
14. Z.Q. Liu, R. Niu, Y.D. Wu, B.K. Li, Y. Gan, and M.H. Wu: *Int. J. Heat Mass Transf.*, 2021, vol. 173, p. 121237. <https://doi.org/10.1016/j.ijheatmasstransfer.2021.121237>.
15. C.J. Wang, Z.Q. Liu, and B.K. Li: *Int. J. Heat Mass Transf.*, 2022, vol. 194, p. 122974. <https://doi.org/10.1016/j.ijheatmasstransfer.2022.122974>.
16. L. Hachani, K. Zaidat, and Y. Fautrelle: *Int. J. Heat Mass Transf.*, 2015, vol. 85, pp. 438–54. <https://doi.org/10.1016/j.ijheatmasstransfer.2015.01.145>.
17. H.H. Ge, F.L. Ren, J. Li, X.J. Han, M.X. Xia, and J.G. Li: *Metall. Mater. Trans. A*, 2017, vol. 48A, pp. 1139–50. <https://doi.org/10.1007/s11661-016-3910-z>.
18. J. Li, M.H. Wu, A. Ludwig, and A. Kharicha: *Int. J. Heat Mass Transf.*, 2014, vol. 72, pp. 668–79. <https://doi.org/10.1016/j.ijheatmasstransfer.2013.08.079>.
19. M.H. Wu, J. Domitner, and A. Ludwig: *Metall. Mater. Trans. A*, 2012, vol. 43A, pp. 945–64. <https://doi.org/10.1007/s11661-011-0940-4>.
20. D.B. Jiang and M.Y. Zhu: *Metall. Mater. Trans. B*, 2016, vol. 47, pp. 3446–58. <https://doi.org/10.1007/s11663-016-0772-0>.
21. D.B. Jiang and M.Y. Zhu: *Metall. Mater. Trans. B*, 2017, vol. 48B, pp. 444–55. <https://doi.org/10.1007/s11663-016-0864-x>.
22. D.B. Jiang, W.L. Wang, S. Luo, C. Ji, and M.Y. Zhu: *Metall. Mater. Trans. B*, 2017, vol. 48B, pp. 3120–31. <https://doi.org/10.1007/s11663-017-1104-8>.
23. R. Guan, C. Ji, M.Y. Zhu, and S.M. Deng: *Metall. Mater. Trans. B*, 2018, vol. 49B, pp. 2571–83. <https://doi.org/10.1007/s11663-018-1352-2>.
24. J. Lipton, M.E. Glicksman, and W. Kurz: *Mater. Sci. Eng.*, 1984, vol. 65, pp. 57–63. [https://doi.org/10.1016/0025-5416\(84\)90199-x](https://doi.org/10.1016/0025-5416(84)90199-x).
25. T. Wang, S. Semenov, E.G. Wang, Y. Delannoy, Y. Fautrelle, and O. Budenkova: *Metall. Mater. Trans. B*, 2019, vol. 50B, pp. 3039–54. <https://doi.org/10.1007/s11663-019-01703-z>.
26. A. Vakhrushev, M.H. Wu, A. Ludwig, Y. Tang, G. Hackl, and G. Nitzl: *Metall. Mater. Trans. B*, 2014, vol. 45B, pp. 1024–37. <https://doi.org/10.1007/s11663-014-0030-2>.
27. A. Ludwig and M.H. Wu: *Metall. Mater. Trans. A*, 2002, vol. 33A, pp. 3673–83. <https://doi.org/10.1007/s11661-002-0241-z>.
28. Y.J. Zheng, M.H. Wu, A. Kharicha, and A. Ludwig: *Modell. Simul. Mater. Sci. Eng.*, 2018, vol. 26, p. 015004. <https://doi.org/10.1088/1361-651X/aa86c5>.

29. C.M.G. Rodrigues, M.H. Wu, H.J. Zhang, A. Ludwig, and A. Kharicha: *Metall. Mater. Trans. A*, 2021, vol. 52A, pp. 4609–622. <https://doi.org/10.1007/s11661-021-06414-2>.
30. M.H. Wu, A. Fjeld, and A. Ludwig: *Comput. Mater. Sci.*, 2010, vol. 50, pp. 32–42. <https://doi.org/10.1016/j.commatsci.2010.07.005>.
31. T. Takaki, S. Sakane, M. Ohno, Y. Shibuta, and T. Aoki: *Acta Mater.*, 2019, vol. 164, pp. 237–49. <https://doi.org/10.1016/j.actamat.2018.10.039>.
32. Y. Mitsuyama, T. Takaki, S. Sakane, Y. Shibuta, and M. Ohno: *Acta Mater.*, 2020, vol. 188, pp. 282–87. <https://doi.org/10.1016/j.actamat.2020.02.016>.
33. C.Y. Wang, S. Ahuja, C. Beckermann, and H.C. Degroh: *Metall. Mater. Trans. B*, 1995, vol. 26B, pp. 111–19. <https://doi.org/10.1007/Bf02648984>.
34. B. Petrus, K. Zheng, X. Zhou, B.G. Thomas, and J. Bentsman: *Metall. Mater. Trans. B*, 2011, vol. 42B, pp. 87–103. <https://doi.org/10.1007/s11663-010-9452-7>.
35. Thermo-Calc Software TCFE7 Steels/Fe-alloys Database, <https://thermocalc.com/products/databases/steel-and-fe-alloys/>.
36. K. Timmel, S. Eckert, G. Gerbeth, F. Stefani, and T. Wondrak: *ISIJ Int.*, 2010, vol. 50, pp. 1134–41. <https://doi.org/10.2355/isijinternational.50.1134>.
37. E. Cadirli and M. Gunduz: *J. Mater. Sci.*, 2000, vol. 35, pp. 3837–48. <https://doi.org/10.1023/A:1004829413966>.
38. R. Moreau: *Magnetohydrodynamics*, Kluwer Academic Publishers, Norwell, 1990.
39. K. Cukierski and B.G. Thomas: *Metall. Mater. Trans. B*, 2008, vol. 39B, pp. 94–107. <https://doi.org/10.1007/s11663-007-9109-3>.
40. J.E. Camporredondo, A.H. Castillejos, F.A. Acosta, E.P. Gutiérrez, and M.A. Herrera: *Metall. Mater. Trans. B*, 2004, vol. 35B, pp. 541–60. <https://doi.org/10.1007/s11663-004-0054-0>.

Publisher's Note Springer Nature remains neutral with regard to jurisdictional claims in published maps and institutional affiliations.

Springer Nature or its licensor (e.g. a society or other partner) holds exclusive rights to this article under a publishing agreement with the author(s) or other rightsholder(s); author self-archiving of the accepted manuscript version of this article is solely governed by the terms of such publishing agreement and applicable law.